Northumbria Research Link

Citation: Qu, Yuwei, Yuan, Jinhui, Zhou, Xian, Li, Feng, Yan, Binbin, Wu, Qiang, Wang, Kuiru, Sang, Xinzhu, Long, Keping and Yu, Chongxiu (2020) Surface Plasmon Resonance-Based Silicon Dual-Core Photonic Crystal Fiber Polarization Beam Splitter at Mid-Infrared Spectral Region. Journal of the Optical Society of America B, 37 (8). pp. 2221-2230. ISSN 0740-3224

Published by: Optical Society of America

URL: https://doi.org/10.1364/josab.396410 <https://doi.org/10.1364/josab.396410>

This version was downloaded from Northumbria Research Link: http://nrl.northumbria.ac.uk/id/eprint/43496/

Northumbria University has developed Northumbria Research Link (NRL) to enable users to access the University's research output. Copyright © and moral rights for items on NRL are retained by the individual author(s) and/or other copyright owners. Single copies of full items can be reproduced, displayed or performed, and given to third parties in any format or medium for personal research or study, educational, or not-for-profit purposes without prior permission or charge, provided the authors, title and full bibliographic details are given, as well as a hyperlink and/or URL to the original metadata page. The content must not be changed in any way. Full items must not be sold commercially in any format or medium without formal permission of the copyright holder. The full policy is available online: http://nrl.northumbria.ac.uk/policies.html

This document may differ from the final, published version of the research and has been made available online in accordance with publisher policies. To read and/or cite from the published version of the research, please visit the publisher's website (a subscription may be required.)

Northumbria
University
NEWCASTLE

CUSTOMER SERVICE EXCELLENCE CSE UniversityLibrary

Surface Plasmon Resonance-Based Silicon Dual-Core Photonic Crystal Fiber Polarization Beam Splitter at Mid-Infrared Spectral Region

YUWEI QU,[1] JINHUI YUAN,[1,2,5] XIAN ZHOU,[2] FENG LI,[3] BINBIN YAN,[1] QIANG WU,[4,6] KUIRU WANG,[1] XINZHU SANG,[1] KEPING LONG,[2] AND CHONGXIU YU[1]

[1] *State Key Laboratory of Information Photonics and Optical Communications, Beijing University of Posts and Telecommunications, Beijing 100876, China*
[2] *Research Center for Convergence Networks and Ubiquitous Services, University of Science & Technology Beijing, Beijing 100083, China*
[3] *Photonics Research Centre, Department of Electronic and Information Engineering, The Hong Kong Polytechnic University, Hung Hom, Hong Kong*
[4] *Department of Physics and Electrical Engineering, Northumbria University, Newcastle upon Tyne, NE1 8ST, United Kingdom*
[5] *yuanjinhui81@bupt.edu.cn*
[6] *qiang.wu@northumbria.ac.uk*

Abstract: In this paper, a novel silicon dual-core photonic crystal fiber (Si-DC-PCF) polarization beam splitter (PBS) based on surface plasmon resonance effect is proposed. The mode coupling characteristics between the X and Y-polarized even and odd modes and surface plasmon polariton mode are analyzed by using the finite element method and coupled-mode theory. The influences of the structure parameters of the Si-DC-PCF on the coupling length and coupling length ratio are investigated. The normalized output power of the X and Y-polarized modes in the cores A and B and the corresponding extinction ratio are also discussed. By optimizing the structure parameters of the Si-DC-PCF, the PBS length of 192 μm and bandwidth of 830 and 730 nm in the cores A and B are achieved. It is believed that the proposed Si-DC-PCF PBS can find important applications in the mid-infrared laser and sensing systems.

1. Introduction

Polarization beam splitter (PBS) is an important device in optical systems [1-5]. It can separate two beams of orthogonal polarized light into two different propagation paths [6], and have important applications in the fields of fiber laser, optical communication, and sensing [7-11]. With the development of the photonic crystal fiber (PCF), many researchers have focused on the PBS based on the dual-core PCF (DC-PCF) [12-16]. In 2010, Chiang et al. reported a DC-PCF PBS, whose fiber length and extinction ratio were 0.3 mm and 23 dB at wavelength 1.55 μm, respectively [17]. In 2014, Jiang et al. proposed a novel DC-PCF PBS, whose fiber length was 119.1 μm and bandwidth was 249 nm [18].

In recent years, the surface plasmon resonance (SPR) technology has gradually been becoming maturity [19-23]. Many investigations on the combination of the PCF and SPR effect for the optical devices have been reported [24-28]. Until now, researchers have designed some DC-PCF PBSs based on the mode coupling between the core mode of the DC-PCF and surface plasmon polariton (SPP) mode [29-33]. In 2019, Rahman et al. demonstrated a kind of DC-PCF PBS with the gold wire filled in the air hole, where the fiber length was only 56.33 μm and bandwidth was up to 530 nm [34]. In 2019, Zhao et al. investigated a SPR-based DC-PCF PBS with the double elliptical air holes, where the fiber length was 104 μm and bandwidth was up to 575 nm [35]. In the previous works, because the substrate materials of the DC-PCF PBS are the silica, the PBS can only be used in the near-infrared optical systems. As the mid-infrared optics and photonics are developed, the fiber devices which are operated in the mid-infrared spectral region have been attracting great interest [36-40]. In 2018, Maes et al. designed a heavily doped holmium fluoride fiber laser which works at wavelength 3.92 μm [41]. In 2020, we proposed a silicon PCF polarization filter with a bandwidth of 2.75 to 7.80 μm [42]. Up to now, the research on the mid-infrared silicon DC-PCF (Si-DC-PCF) PBS has not been reported.

In this paper, we propose a novel Si-DC-PCF PBS based on the mode coupling theory and SPR effect. The coupling length in the X-polarized (X-pol) and Y-polarized (Y-pol) directions and the corresponding coupling length ratio are analyzed, and the normalized output power and extinction ratio of the cores A and B are also discussed. The PBS length of 192 μm and bandwidth of 830 and 730 nm in the cores A and B are achieved.

2. Design of the Si-DC-PCF PBS

The cross-section structure and schematic diagram of the practical application in the optical system of the designed Si-DC-PCF PBS are shown in Figs. 1(a) and 1(b), respectively. From Fig. 1(a), the background material of the Si-DC-PCF is the pure silicon. The Si-DC-PCF is missing the two air holes in the X direction to form the cores A and B. The Si-DC-PCF includes four kinds of air holes with the different sizes. The diameter of the air hole between the cores A and B is d_1, and the gold film with a thickness of t is coated in this air hole. The diameter of the two small air holes on the left side of the core A and the right side of the core B is d_2. The diameter of the eight air holes above and below the cores A and B is d_3. The diameter of the other air holes is d_4, and the hole-to-hole pitch is Λ. The finite element method (FEM) is used. A perfect matching layer (PML) is set at the outermost layer of the designed Si-DC-PCF to absorb the radiation energy, and the refractive index of the PML is 0.03 higher than that of the pure silicon [43]. From Fig. 1(b), after passing through the designed Si-DC-PCF PBS, the orthogonal polarized light emitted from the light source is completely separated into the two beams of polarized light. The two beams of polarized light can be launched into the different optical systems, such as laser and sensor systems.

The material dispersion of the pure silicon is described by the Sellmeier equation [44]

$$n_{\mathrm{Si}}(\lambda) = \varepsilon + \frac{\mathrm{A}}{\lambda^2} + \frac{\mathrm{B}\lambda_1^2}{\lambda^2 - \lambda_1^2}, \tag{1}$$

where λ_1=1.1071 μm, ε=11.6858, A=0.939816 μm^2, and B=8.10461×10^{-3}.

The relative dielectric constant of the gold film can be described by the Drude-Lorentz model [45]

$$\varepsilon_{\mathrm{m}} = \varepsilon_{\infty} - \frac{\omega_{\mathrm{D}}^2}{\omega(\omega - j\gamma_{\mathrm{D}})} - \frac{\Delta\varepsilon \cdot \Omega_{\mathrm{L}}^2}{(\omega^2 - \Omega_{\mathrm{L}}^2) - j\Gamma_{\mathrm{L}}\omega}, \tag{2}$$

where ε_{∞}=5.9673 and $\Delta\varepsilon$=1.09 are the high frequency dielectric constant and weighted coefficient, respectively, ω, ω_{D}, and γ_{D} are the angle frequency of the guided-wave, plasma frequency, and damping frequency, respectively, Ω_{L} represents the frequency of the Lorentz oscillator, and Γ_{L} represents the bandwidth of the Lorentz oscillator. In this work, $\omega_{\mathrm{D}}/2\pi$=2113.6 THz, $\gamma_{\mathrm{D}}/2\pi$=15.92 THz, $\Omega_{\mathrm{L}}/2\pi$=650.07 THz, and $\Gamma_{\mathrm{L}}/2\pi$=104.86 THz.

The coupling length (CL) in the different polarization directions can be calculated by [46]

$$CL_{\mathrm{X}} = \frac{\lambda}{2\left|(n_{\mathrm{even}}^{\mathrm{X}} - n_{\mathrm{odd}}^{\mathrm{X}})\right|}, \tag{3}$$

$$CL_{\mathrm{Y}} = \frac{\lambda}{2\left|(n_{\mathrm{even}}^{\mathrm{Y}} - n_{\mathrm{odd}}^{\mathrm{Y}})\right|}, \tag{4}$$

where CL_{X} and CL_{Y} are the coupling length of the X-pol and Y-pol, respectively, λ is the wavelength of the incident light, and *n*X even , *n*X odd , *n*Y even and *n*Y odd are the effective refractive indices of the even and odd modes in the X-pol and Y-pol, respectively.

The coupling length ratio (*CLR*) can be described by [47]

$$CLR = \frac{CL_{\mathrm{Y}}}{CL_{\mathrm{X}}}, \tag{5}$$

When the *CLR*=2 or 1/2, the polarization splitting length is the optimum value.

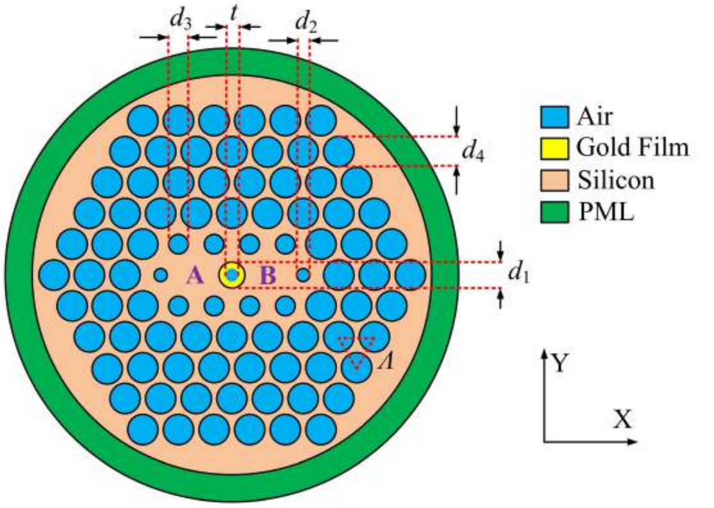

(a)

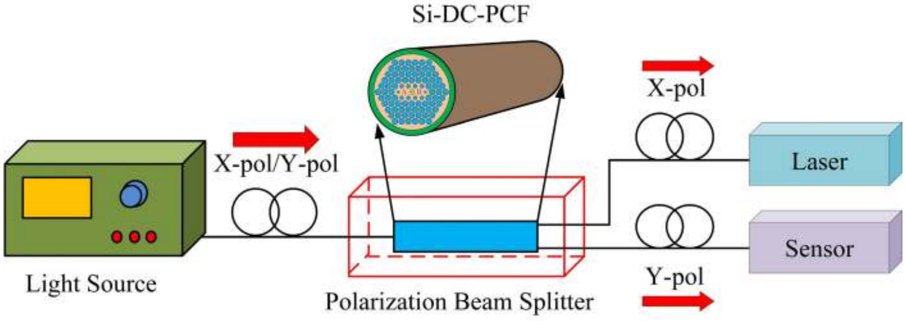

(b)

Fig. 1. (a) The cross-section structure of the designed Si-DC-PCF PBS, and (b) the schematic diagram of the practical application in the optical systems.

The normalized output powers (P_{out}) of the X-pol and Y-pol in the cores A and B can be described by [48]

$$P_{\mathrm{out,\,A}}^{\mathrm{X,\,Y}} = P_{\mathrm{in}} \cos^2\left(\frac{\pi}{2}\frac{L_{\mathrm{P}}}{CL_{\mathrm{X,\,Y}}}\right), \tag{6}$$

$$P_{\mathrm{out,\,B}}^{\mathrm{X,\,Y}} = P_{\mathrm{in}} \sin^2\left(\frac{\pi}{2}\frac{L_{\mathrm{P}}}{CL_{\mathrm{X,\,Y}}}\right), \tag{7}$$

where P_{in} is the input power and L_{p} is the propagation length of the designed Si-DC-PCF.

The extinction ratio (*ER*) of the cores A and B as an important parameter to determine the splitter quality can be expressed as [49]

$$ER_{\mathrm{A}} = 10\log_{10}\frac{P_{\mathrm{out,\,A}}^{\mathrm{X}}}{P_{\mathrm{out,\,A}}^{\mathrm{Y}}}, \tag{8}$$

$$ER_{\mathrm{B}} = 10\log_{10}\frac{P_{\mathrm{out,\,B}}^{\mathrm{Y}}}{P_{\mathrm{out,\,B}}^{\mathrm{X}}}, \tag{9}$$

The wavelength range with the *ER* larger than 20 dB can be considered as the splitting bandwidth of the PBS. Because the cores A and B of the designed Si-DC-PCF have the same structure and symmetry, we only need to consider the change of P_{out} along the X-pol and Y-pol directions and *ER* in the cores A and B when the input light is propagated in the core A at the initial stage.

3. Simulation results and discussion

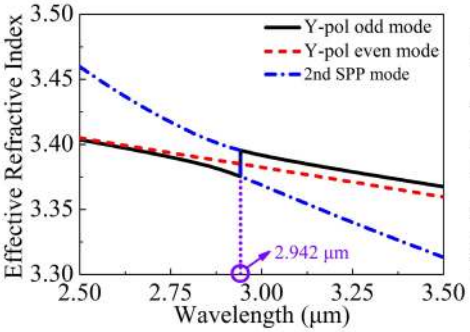

(a) (b)

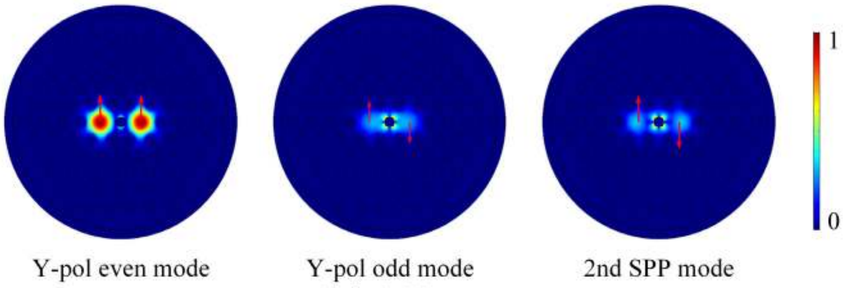

(c) λ=2.942 μm

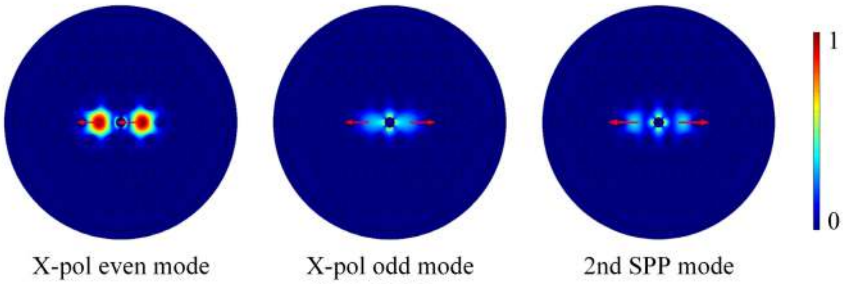

(d) λ=3.020 μm

Fig. 2. The effective refractive indices of (a) Y-pol and (b) X-pol even and odd modes and 2nd SPP mode, and the mode field distributions of (c) the Y-pol even and odd modes and 2nd SPP mode at wavelength 2.942 μm and (d) the X-pol even and odd modes and 2nd SPP mode at wavelength 3.020 μm.

When the initial structure parameters of the designed Si-DC-PCF are set as d_1=1.08 μm,

d_2=1.00 μm, d_3=1.05 μm, d_4=1.20 μm, Λ=2.2 μm, and t=45 nm, the effective refractive indices of the Y-pol and X-pol even and odd modes and 2nd SPP mode calculated by the FEM are shown in Figs. 2(a) and 2(b), respectively. From Fig. 2(a), the effective refractive indices of the Y-pol odd mode and 2nd SPP mode have a resonant point at wavelength 2.942 μm, while the effective refractive indices of the Y-pol even mode and 2nd SPP mode don't have resonant point. From Fig. 2(b), the effective refractive indices of the X-pol odd mode and 2nd SPP mode have a resonant point at wavelength 3.020 μm, while the effective refractive indices of the X-pol even mode and 2nd SPP mode don't have resonant point. According to the coupled-mode theory [50, 51], the complete coupling between the Y-pol and X-pol odd modes and 2nd SPP mode occur at wavelengths 2.942 and 3.020 μm, respectively, while there are no mode coupling between the Y-pol and X-pol even modes and 2nd SPP within the wavelength range considered. The mode field distributions of the Y-pol and X-pol modes and 2nd SPP mode are shown in Figs. 2(c) and 2(d), respectively. From Figs. 2(c) and 2(d), the mode field energy of the Y-pol and X-pol even modes does not change at wavelengths 2.942 and 3.020 μm. However, the mode field energy of the Y-pol and X-pol odd modes and 2nd SPP mode occurs to strongly transfer at wavelengths 2.942 and 3.020 μm. Therefore, it is further confirmed that the complete coupling between the Y-pol and X-pol odd modes and 2nd SPP mode occur at wavelengths 2.942 and 3.020 μm.

The CL of the Y-pol (CL_Y) and X-pol (CL_X) and CLR of the designed Si-DC-PCF are shown in Fig. 3. It can be seen from Fig. 3 that the CL_Y and CL_X have mutation inflection points at wavelengths 2.942 and 3.020 μm, respectively, which correspond to the resonant points of the effective refractive indices of the Y-pol and X-pol odd modes. This results in the sudden changes of the effective refractive index differences between the Y-pol and X-pol odd and even modes. After wavelengths 2.942 and 3.020 μm, the changes of the CL_Y and CL_X keep stable as the wavelength increases. After wavelength 3.020 μm, the CLR remains ~1.85 as the wavelength increases. In order to obtain the optimized polarization splitting length (CLR=2), we will analyze the influences of the structure parameters of the designed Si-DC-PCF on the CL_Y, CL_X, and CLR.

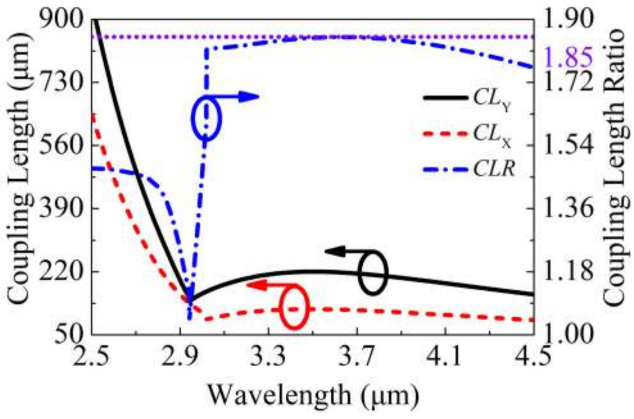

Fig. 3. The CL of the Y-pol (CL_Y) and X-pol (CL_X) and CLR of the designed Si-DC-PCF.

Figs. 4(a), 4(b), and 4(c) show the relationships between the CL_Y, CL_X, and CLR and d_1, respectively. From Figs. 4(a) and 4(b), with the increase of d_1, the CL_Y and CL_X decrease gradually at the shorter wavelength at the same time, but the relative decrease of the CL_Y is smaller than that of the CL_X. Moreover, the CL_Y and CL_X change less at the longer wavelength, and the mutation inflection point shifts towards the long wavelength. Consequently, with the increase of d_1, the mutation inflection point of the CLR shifts towards the long wavelength gradually, and the CLR after the mutation inflection point increases stably, as shown in Fig. 4(c).

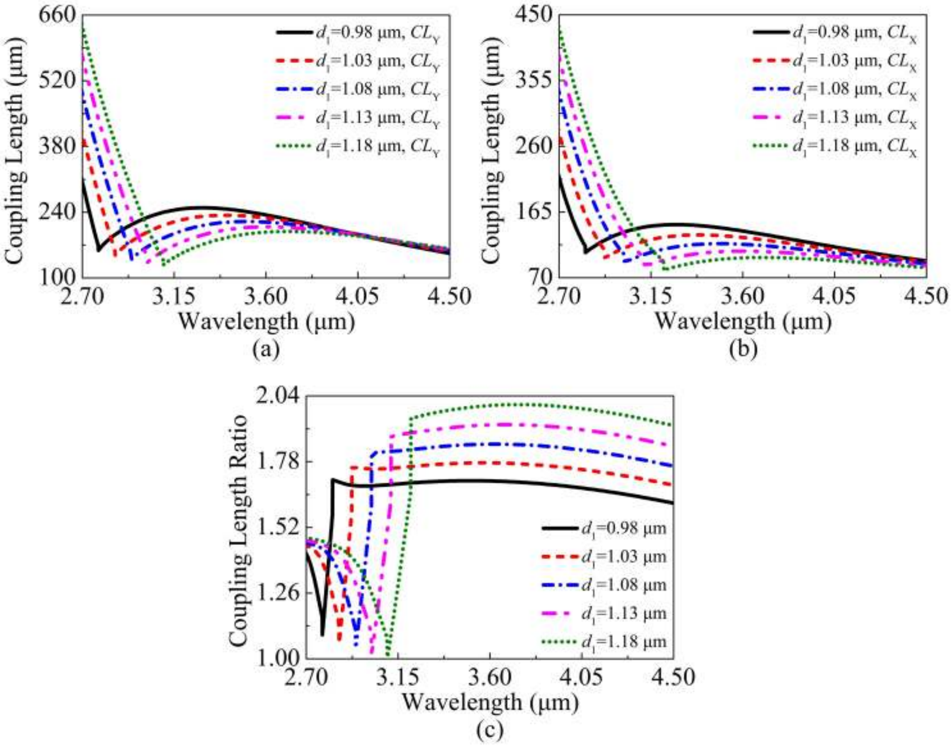

Fig. 4. The relationships between the *CL* of (a) Y-pol and (b) X-pol and (c) *CLR* and d_1.

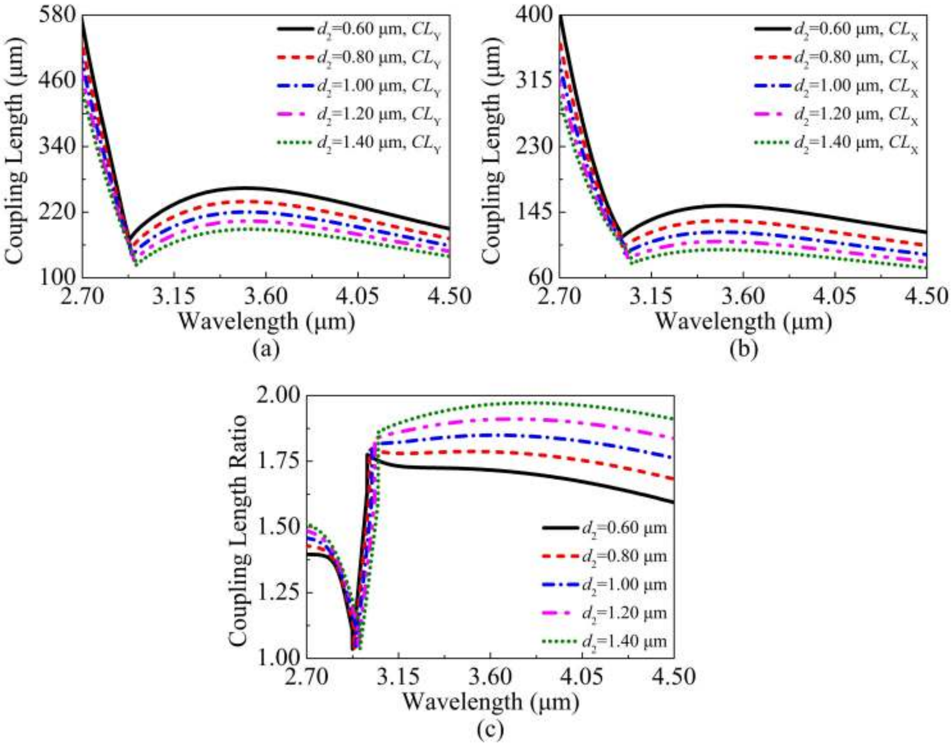

Fig. 5. The relationships between the *CL* of (a) Y-pol, (b) X-pol, and (c) *CLR* and d_2.

The relationships between the CL_{Y}, CL_{X}, and *CLR* and d_2 are shown in Figs. 5(a), 5(b), and 5(c), respectively. In Figs. 5(a) and 5(b), as d_2 increases, the CL_{Y} and CL_{X} decrease gradually at the shorter wavelength, but the relative decrease of the CL_{Y} is smaller than that of the CL_{X}. Moreover, the mutation inflection point slightly shifts towards the long wavelength. As a result, when d_2 increases, the mutation inflection point of the *CLR* slightly shifts towards the long wavelength, and the *CLR* after the mutation inflection point increases gradually, as shown in Fig. 5(c).

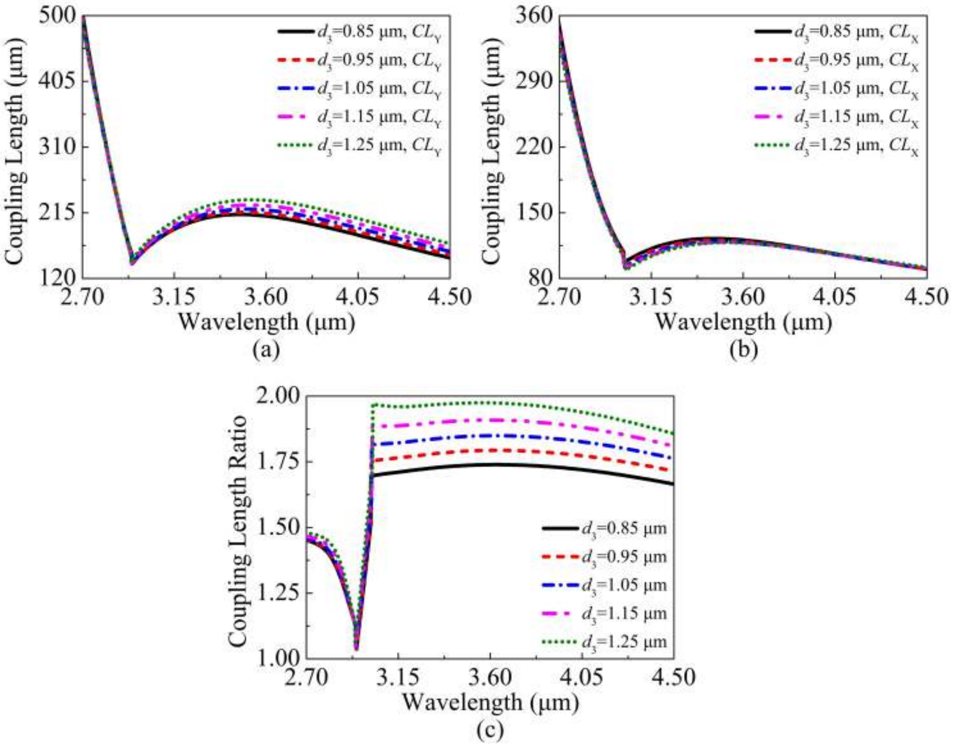

(a) (b)

(c)

Fig. 6. The relationships between the *CL* of (a) Y-pol, (b) X-pol, and (c) *CLR* and d_3.

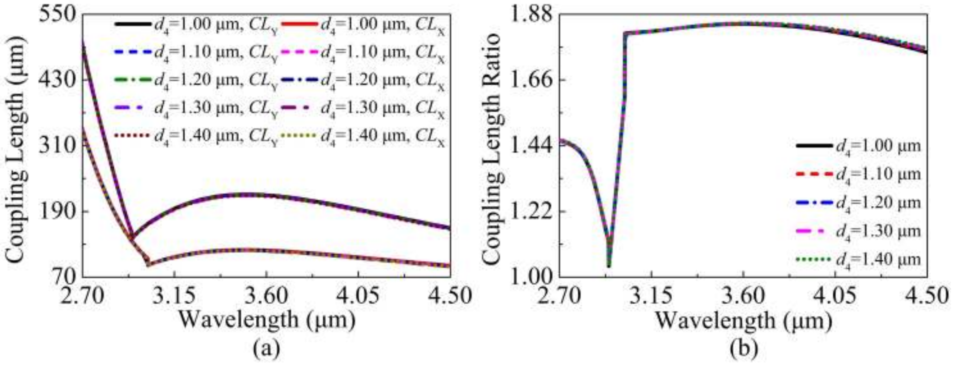

(a) (b)

Fig. 7. The relationships between (a) the *CL* of the Y-pol and X-pol, (b) *CLR* and d_4.

Figs. 6(a), 6(b), and 6(c) show the relationships between the CL_{Y}, CL_{X}, and *CLR* and d_3, respectively. It can be seen from Figs. 6(a) and 6(b) that the CL_{Y} increases gradually, but the CL_{X} changes slightly when d_3 increases. And the mutation inflection point remains nearly unchanged. Thus, as d_3 increases, the mutation inflection point of the *CLR* remains nearly unchanged, and the *CLR* after the mutation inflection point retains a relatively stable increase, as shown in Fig. 6(c).

Figs. 7(a) and 7(b) show the relationships between the CL_Y, CL_X, and *CLR* and d_4, respectively. From Fig. 7(a), the CL_Y and CL_X change slightly when d_4 increases. The main reason is considered that the influences of d_4 on the effective refractive indices of the even and odd modes of the Y-pol and X-pol have reached an approximate convergence. Therefore, the *CLR* remains nearly unchanged with the increase of d_4, as seen from Fig. 7(b).

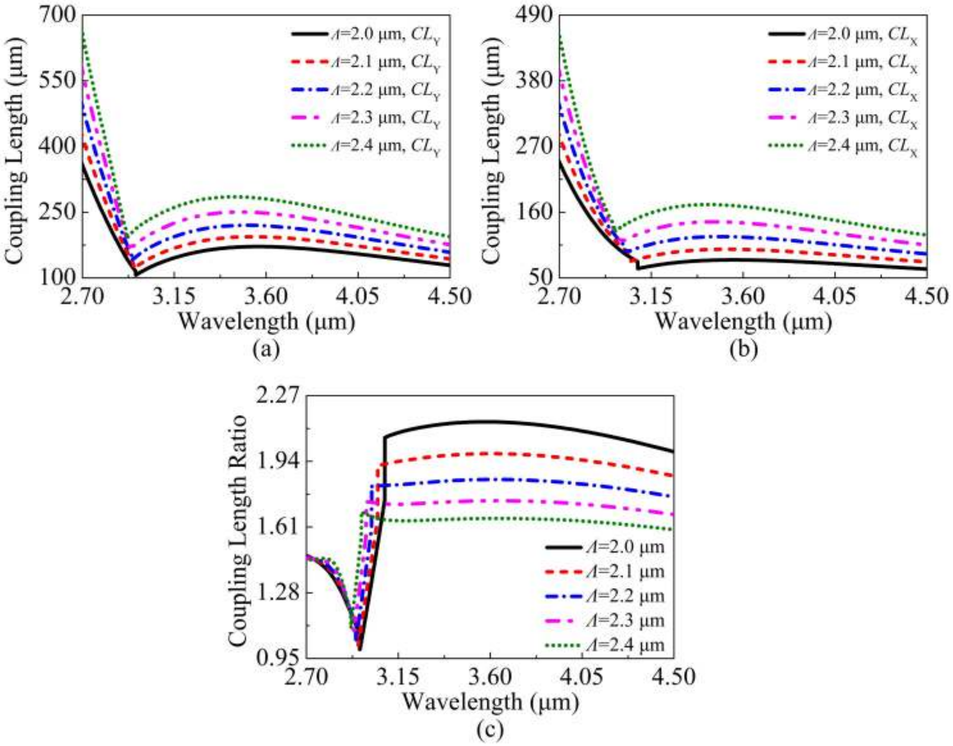

Fig. 8. The relationships between the *CL* of (a) Y-pol, (b) X-pol, and (c) *CLR* and *Λ*.

The relationships between the CL_Y, CL_X, and *CLR* and *Λ* are shown in Figs. 8(a), 8(b), and 8(c), respectively. In Figs. 8(a) and 8(b), with the increase of *Λ*, the CL_Y and CL_X increase gradually, but the relative increase of the CL_Y is smaller than that of the CL_X. In addition, the mutation inflection point occurs to slightly shift towards the short wavelength. Hence, with the increase of *Λ*, the mutation inflection point of the *CLR* has a little shift towards the short wavelength, and the *CLR* after the mutation inflection point maintains a relatively stable decrease, as seen from Fig. 8(c).

Figs. 9(a), 9(b), and 9(c) show the relationships between the CL_Y, CL_X, and *CLR* and *t*, respectively. From Figs. 9(a) and 9(b), as *t* increases, the CL_Y and CL_X increase gradually at the shorter wavelength, but the relative increase of the CL_Y is smaller than that of the CL_X. In addition, although the CL_Y and CL_X decrease gradually at the longer wavelength, the relative decrease of the CL_Y is larger than that of the CL_X, and the mutation inflection point shifts towards the short wavelength. It can also be seen from Figs. 9(a) and 9(b) that the values of the CL_Y and CL_X change in a relatively small range. As a result, with the increase of *t*, the mutation inflection point shifts towards the short wavelength, and the *CLR* after the mutation inflection point decreases gradually in a small range, as seen from Fig. 9(c).

According to the above results, the influences of the structure parameters of the Si-DC-PCF on the CL_Y, CL_X, and *CLR* can be found. Thus, the optimization process of designing the Si-DC-PCF can be summarized as following. First, the *CLR*=2 could be achieved by adjusting Λ, d_1, and d_3. Second, a suitable mutation inflection point at the short wavelength can be obtained by adjusting t. Third, the flatness of the *CLR* can be changed by adjusting d_2 and d_4. Finally, the structure parameters of the designed Si-DC-PCF are optimized as follows: d_1=1.25 μm, d_2=1.00 μm, d_3=1.00 μm, d_4=1.20 μm, Λ=2.25 μm, and t=50 nm. At this time, the corresponding CL_Y, CL_X, *CLR*, and *CLR* in the wavelength range from 3.35 to 4.35 μm are shown in Figs. 10(a) and 10(b), respectively. From Fig. 10(a), the CL_Y and CL_X have a mutation inflection point at wavelengths 3.124 and 3.255 μm, respectively. After 3.255 μm, the value of the *CLR* remains ~ 2 in a wide wavelength range. From Fig. 10(b), the value of the *CLR* remains in the range of 1.96 ~ 2.01 in the wavelength range from 3.35 to 4.35 μm.

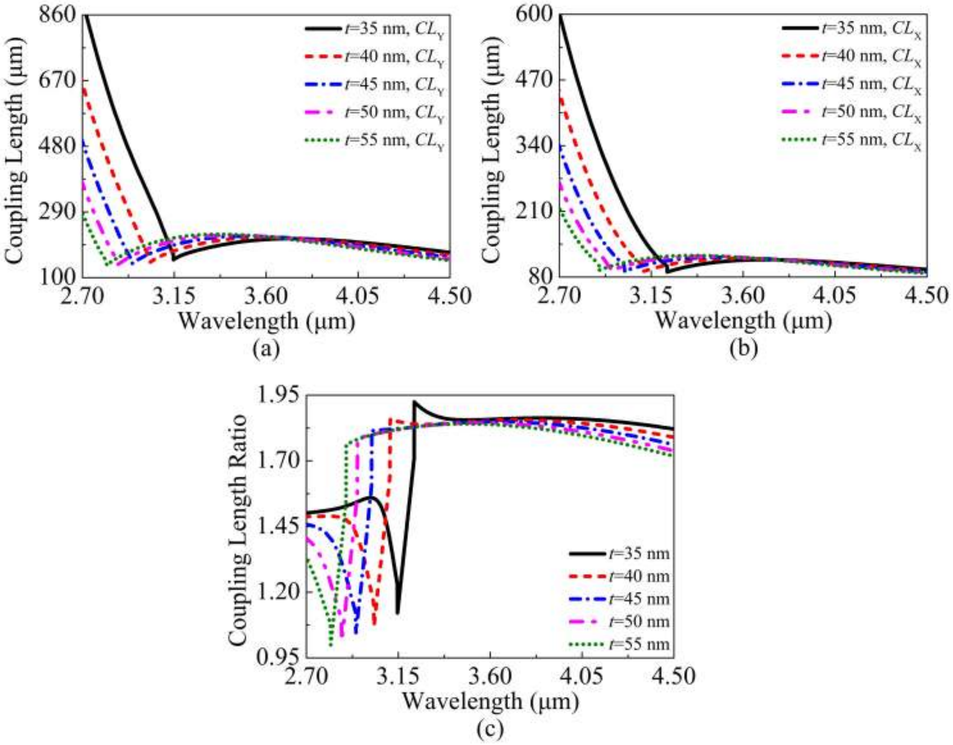

Fig. 9. The relationships between the *CL* of (a) Y-pol, (b) X-pol, and (c) *CLR* and *t*.

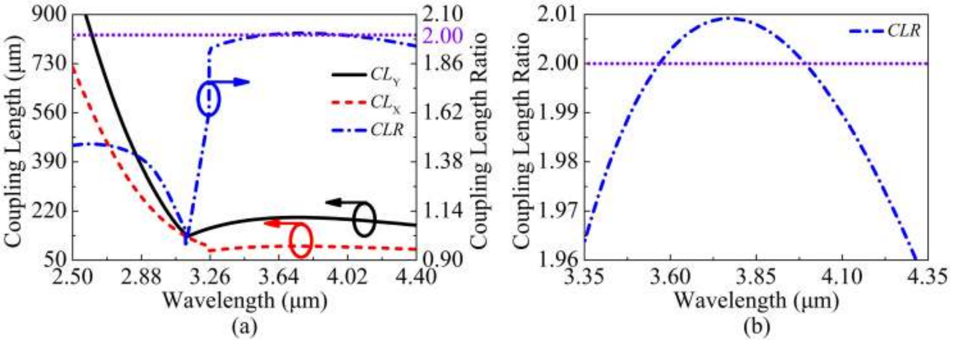

Fig. 10. (a) The final *CL* of the Y-pol and X-pol and *CLR*, and (b) the *CLR* in the wavelength range from 3.35 to 4.35 μm.

It is assumed that the input light is launched into the core A. When the wavelength of the input light is located at 4 μm, the *CLR* is exactly equal to 2. The relationships between P_{out} of the X-pol and Y-pol in the cores A and B and propagation length of the designed Si-DC-PCF at wavelength 4 μm are shown in Figs. 11(a) and 11(b), respectively. From Fig. 11(a), when the propagation length is 192 μm, P_{out} of the X-pol in the core A reaches the maximum once again, while P_{out} of the Y-pol in the core A becomes 0 for the first time, which indicates that only the X-pol light remains in the core A at this time. From Fig. 11(b), when the propagation length is 192 μm, P_{out} of the Y-pol in the core B reaches the maximum for the first time, but P_{out} of the X-pol in the core B becomes 0 once again, which indicates that only the Y-pol light remains in the core B at this time. Therefore, the polarization splitting length of the designed Si-DC-PCF is 192 μm. In addition, it can also be observed from Figs. 11(a) and 11(b) that the normalized output power decreases slightly with the increase of the propagation length, which is mainly induced by the ohmic loss of the gold film since a fraction of energy is propagated on the gold film surface [52].Then, when the polarization splitting length is 192 μm, the *ER* of the cores A and B as functions of the wavelength are shown in Figs. 12(a) and 12(b), respectively. From Fig. 12(a), the *ER* of the core A achieves 61.48 and 62.69 dB at wavelengths 3.52 and 4.01 μm, respectively, and the corresponding bandwidth with the *ER* larger than 20 dB in the core A is 830 nm (3.40 ~ 4.23 μm). The *ER* of the core B achieves 53.74 and 61.78 dB at wavelengths 3.51 and 4.01 μm, respectively, and the corresponding bandwidth with the *ER* larger than 20 dB in the core B is 730 nm (3.4 ~ 4.16 μm), as shown in Fig. 12(b).

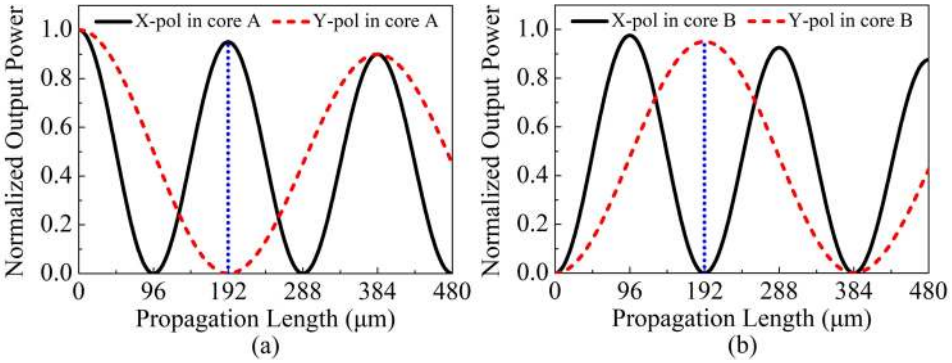

Fig. 11. The relationships between the normalized output power P_{out} of the X-pol and Y-pol in the (a) core A and (b) core B and propagation length of the designed Si-DC-PCF at wavelength 4 μm.

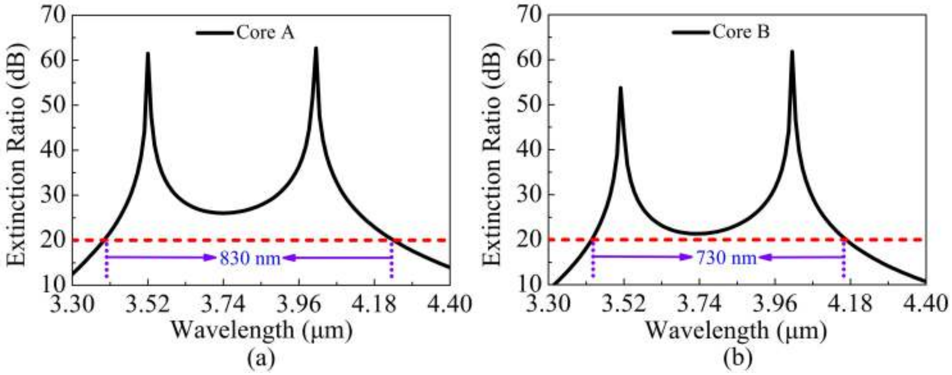

Fig. 12. The *ER* of (a) core A and (b) core B as functions of the wavelength.

Table 1 shows the comparison results between the proposed Si-DC-PCF PBS and reported

DC-PCF PBS. From Table 1, although the length of the proposed Si-DC-PCF PBS is slightly longer than that in Refs [48] and [34], the proposed fiber structure is a traditional hexagonal lattice, which is easy to fabricate. In addition, the proposed Si-DC-PCF PBS has the two large bandwidths at mid-infrared spectral region. The bandwidths with the *ER* above 20 dB in the cores A and B can be up to 830 and 730 nm, respectively.

Table 1. Comparison results between the proposed Si-DC-PCF PBS and reported DC-PCF PBS.

Reference	Additional materials or other structures	PBS length	Bandwidth of *ER* above 20 dB in core A	Bandwidth of *ER* above 20 dB in core B
[30] 2015	Gold film	542 μm	210 nm (~ E+S+C+L)	220 nm (~ E+S+C+L)
[13] 2016	Liquid crystal (E7)	890.5 μm	~ 150 nm (~ S+C+L)	Not mentioned
[14] 2017	Gold wire	1079 μm	70 nm	Not mentioned
[16] 2017	magnetic fluids	8130 μm	Not mentioned	Not mentioned
[48] 2018	Rectangular lattice	103 μm	177 nm (1.458 ~ 1.635 μm)	79 nm (1.508 ~ 1.587 μm)
[34] 2019	Gold film and Rectangular lattice	104 μm	575 nm (1.35 ~ 1.925 μm)	Not mentioned
This work	Gold film	192 μm	830 nm (3.40 ~ 4.23 μm)	730 nm (3.43 ~ 4.16 μm)

At present, the proposed Si-DC-PCF can be fabricated by the stack and draw technology combined with the magnesium thermal reduction or femtosecond laser drilling method [53, 54]. The gold film can be deposited by the high pressure microfluidic chemical deposition [57-60].

4. Conclusions

In summary, a novel Si-DC-PCF PBS based on the SPR effect is proposed. By optimizing the structure parameters of the Si-DC-PCF, the *CLR* remains in the range of 1.96 ~ 2.01 in the wavelength range from 3.35 to 4.35 μm. When the polarization splitting length is chosen as 192 μm, only the X-pol light remains in the core A, and the corresponding Y-pol light remains in the core B. The *ER*s of the cores A and B achieve 61.48 and 62.69 dB, and 53.74 and 61.78 dB at wavelengths 3.52 and 4.01 μm, and 3.51 and 4.01 μm, respectively. The bandwidths with the *ER* larger than 20 dB in the cores A and B can be up to 830 nm (3.40 ~ 4.23 μm) and 730 nm (3.43 ~ 4.16 μm), respectively. The proposed Si-DC-PCF PBS has the ultra-short polarization splitting length and ultra-wide splitting bandwidth, so it can be applied in the different mid-infrared optical systems. For example, it can be applied in the holmium-doped fluoride fiber laser system [41].

Funding

National Key Research and Development Project of China (2019YFB2204001) and National Natural Science Foundation of China (61875238 and 61935007).

Acknowledgements

We thank the State Key Laboratory of Information Photonics and Optical Communications (Beijing University of Posts and Telecommunications of China) for the scientific helps and supports throughout this research.

Disclosures

The authors declare no conflicts of interest.

References

1. Y. Xie, Z. X. Chen, J. Yan, Y. H. Wu, T.Y. Huang, and Z. Cheng, "Combination of Surface Plasmon Polaritons and Subwavelength Grating for Polarization Beam Splitting," Plasmonics **15**(1) 235-241 (2020).
2. T. T. Zhao, S. Q. Lou, X. Wang, M. Zhou, and Z. G. Lian, "Ultrabroadband polarization splitter based on three-core photonic crystal fiber with a modulation core," Appl. Opt. **55**(23) 6428-6434 (2016).
3. K. Tan, Y. Huang, G. Q. Lo, C. Y. Yu, and C. K. Lee, "Experimental realization of an O-band compact polarization splitter and rotator," Opt. Express **25**(4) 3234-3241 (2017).
4. L. H. Xu, Y. Wang, E. E. Fiky, D. Mao, A. Kumar, Z. P. Xing, M. G. Saber, M. Jacques, and D. V. Plant, "Compact Broadband Polarization Beam Splitter Based on Multimode Interference Coupler With Internal Photonic Crystal for the SOI Platform," J. Lightw. Technol. **37**(4) 1231-1240 (2019).
5. Q. Liu, S. G. Li, Z. K. Fan, W. Zhang, H. Li, J. C. Zi, and G. W. An, "Numerical analysis of ultrabroadband polarization splitter based on gold-filled dual-core photonic crystal fiber," Opt. Commun. **334** 46-50 (2015).
6. W. L. Lu, S. Q. Lou, X. Wang, L. W. Wang, and R. J. Feng, "Ultrabroadband polarization splitter based on three-core photonic crystal fibers," Appl. Opt. **52**(3) 449-455 (2013).
7. O. Acher and S. Richard, "Easy-to-build Wollaston-like polarization splitter with adjustable beam deviation and tunable chromatic dispersion," Opt. Express **27**(20) 29232-29240 (2019).
8. X. Y. Dai, G. Y. Zhao, Q. A. Chen, Q. Y. Lu, J. F. Donegan, and W. H. Guo, "High-performance InP-based Mach-Zehnder polarization beam splitter with a 19 dB extinction ratio across C-band," Opt. Lett. **44**(17) 4299-4320 (2019).
9. Y. Tian, J. F. Qiu, C. Liu, S. H. Tian, Z. L. Huang, and J. Wu, "Compact polarization beam splitter with a high extinction ratio over S+C+L band," Opt. Express **27**(2) 999-1009 (2019).
10. Z. D. Liu, J. Q. Guo, B. Y. Tian, Y. X. Bian, R. Y. Zhang, and Z. N. Wang, "Omnidirectional polarization beam splitter for white light," Opt. Express **27**(5) 7673-7684 (2019).
11. L. Fang and J. Wang, "All-fiber polarization beam splitting and rotating based on vector-mode-assisted coupling," Opt. Express **26**(12) 15124-15137 (2018).
12. Z. L. Xu, X. Y. Li, W. W. Ling, P. Liu, and Z. Y. Zhang, "Design of short polarization splitter based on dual-core photonic crystal fiber with ultra-high extinction ratio," Opt. Commun. **354** 314-320 (2015).
13. E. L. Wang, H. M. Jiang, K. Xie, C. Chen, and Z. J. Hu, "Polarization splitter based on dual core liquid crystal-filled holey fiber," J. Appl. Phys. **120** 114501 (2016).
14. X. Y. Wang, S. G. Li, Q. Liu, Z. K. Fan, G. Y. Wang, and Y. Y. Zhao, "High-extinction ratio and short-length polarization splitter based on microstructured optical fiber with tellurite glass," Opt. Mater. **66** 542-546 (2017).
15. B. M. Younis, A. M. Heikal, M. F. O. Hameed, and S. S. A. Obayya, "Highly wavelength-selective asymmetric dual-core liquid photonic crystal fiber polarization splitter," J. Opt. Soc. Am. B **35**(5) 1020-1028 (2018).
16. J. H. Wang, L. Pei, S. J. Weng, L. Y. Wu, L. Huang, T. G. Ning, and J. Li, "A Tunable Polarization Beam Splitter Based on Magnetic Fluids-Filled Dual-Core Photonic Crystal Fiber," IEEE Photo. J. **9**(1) 2200410 (2017).
17. J. S. Chiang, N. H. Sun, S. C. Lin, and W. F. Liu, "Analysis of an Ultrashort PCF-Based polarization splitter," J. Lightw. Technol. **28**(5) 707-713 (2010).
18. H. M. Jiang, E. L. Wang, J. Zhang, L. Hu, Q. P. Mao, Q. Li, and K. Xie, "Polarization splitter based on dual-core photonic crystal fiber," Opt. Express **22**(25) 30461-30466 (2014).
19. J. L. Dong, Y. X. Zhang, Y. J. Wang, F. Yang, S. Q. Hu, Y. F. Chen, W. G. Zhu, W. T. Qiu, H. Y. Guan, H. H. Lu, J. H. Yu, Y. C. Zhong, J. Zhang, Y. H. Luo, and Z. Chen, "Side-polished few-mode fiber based surface plasmon resonance biosensor," Opt. Express **27**(8) 11348-11360 (2019).
20. N. A. S. Omar, Y. W. Fen, S. Saleviter, Y. M. Kamil, W. M. E. M. M. Daniyal, J. Abdullah, and M. A.r Mahdi, "Experimental evaluation on surface plasmon resonance sensor performance based on sensitive hyperbranched polymer nanocomposite thin films," Sensor. Actuat. A Phys. **303**(1) 111830 (2020).
21. Q. H. Liu, B. Yan, and J. J. Liu, "U-shaped photonic quasi-crystal fiber sensor with high sensitivity based on surface plasmon resonance," Appl. Phys. Express **12** 052014 (2019).
22. Y. J. Zhang, F. j. Tian, Z. L. Su, R. L. Bai, L. Li, X. H. Yang, and J. Z. Zhang, "Broadband single-polarization optical fiber based on surface plasmon resonance," Appl. Opt. **59**(3) 779-784 (2020).
23. Y. C. Liu, S. G. Li, H. L. Chen, J. S. Li, and W. X. Zhang, "Surface plasmon resonance induced high sensitivity refractive index sensor with adjustable measurement range based on evanescent field enhanced DFPCF," J. Phys. D Appl. Phys. **53** 115107 (2020).
24. C. Liu, L. Yang, Q. Liu, F. M. Wang, Z. J. Sun, T. Sun, H. W. Mu, and P. K. Chu, "Analysis of a Surface Plasmon Resonance Probe Based on Photonic Crystal Fibers for Low Refractive Index Detection," Plasmonics **13** 779-784 (2018).

25. G. W. An, S. G. Li, X. Yan, Z. Y. Yuan, and X. N. Zhang, “High-birefringence photonic crystal fiber polarization filter based on surface plasmon resonance,” Appl. Opt. **55**(6) 1262-1266 (2016).
26. C. Liu, J. W. Wang, F. M. Wang, W. Q. Su, L. Yang, J. W. Lv, G. L. Fu, X. L. Li, Q. Liu, T. Sun, and P. K. Chu, “Surface plasmon resonance (SPR) infrared sensor based on D-shape photonic crystal fibers with ITO coatings.” Opt. Commun. **464** 125496 (2020).
27. M. M. Rahman, A. Khaleque, M. T. Rahman, and F. Rabbi, “Gold-coated photonic crystal fiber based polarization filter for dual communication windows,” Opt. Commun. **461** 125293 (2020).
28. C. Liu, L. Y. Wang, L. Yang, F. M. Wang, C. H. Xu, J. W. Lv, G. L. Fu, X. L. Li, Q. Liu, H. W. Mu, T. Sun, and P. K. Chu, “The single-polarization filter composed of gold-coated photonic crystal fiber,” Phys. Lett. A **383** 3200-3206 (2019).
29. A. Khaleque and H. T. Hattori, “Ultra-broadband and compact polarization splitter based on gold filled dual-core photonic crystal fiber,” J. Appl. Phys. **118** 143101 (2015).
30. Z. K. Fan, S. G. Li, Q. Liu, J. S. Li, and Yang Xie, “Plasmonic Polarization Beam Splitter Based on Dual-Core Photonic Crystal Fiber,” Plasmonics **10** 1283-1289 (2015).
31. L. H. Jiang, Y. Zheng, L. T. Hou, K. Zheng, J. Y. Peng, and X. T. Zhao, “An ultrabraoadband polarization splitter based on square-lattice dual┐ core photonic crystal fiber with a gold wire,” Opt. Commun. **351** 50-56 (2015).
32. P. Li and J. L. Zhao, “Polarization-dependent coupling in gold-filled dual-core photonic crystal fibers,” Opt. Express **21**(5) 5232-5238 (2013).
33. Y. Y. Zhao, S. G. Li, X. Y. Wang, G. Y. Wang, M. Shi, and J. J. Wu, “Design of a novel multi channel photonic crystal fiber polarization beam splitter,” Opt. Commun. **400** 79-83 (2017).
34. M. T. Rahman and A. Khaleque, “Ultra-short polarization splitter based on a plasmonic dual-core photonic crystal fiber with an ultra-broad bandwidth,” Appl. Opt. **58**(34) 9426-9433 (2019).
35. X. T. Zhao, L. Hua, Q. Xiong, G. H. Jiang, and J. R.Cheng, “Ultra-short and broadband polarization splitter based on PCF and metal surface plasmons resonance,” Opt. Quant. Electron. **51** 162 (2019).
36. C. F. Yao, Z. X. Jia, Z. R. Li, S. J. Jia, Z. P. Zhao, L. Zhang, Y. Feng, G. S. Qin, Y. Ohishi, and W. P. Qin, “High-power mid-infrared supercontinuum laser source using fluorotellurite fiber,” Optica **5**(10) 1264-1270 (2018).
37. J. Cui, X. S. Xiao, Y. T. Xu, X. X. Cui, M. L. Chen, J. J. Guo, M. Lu, B. Peng, and H. T. Guo, “Mid-infrared emissions of Dy^{3+} doped Ga-As-S chalcogenide glasses and fibers and their potential for a 4.2 µm fiber laser”, Opt. Mater. Express **8**(8) 2089-2102 (2018).
38. B. Y. Li, M. Wu, X. Y. Liu, G. Y. Zhou, T. Wang, Z. C. Sheng, Z. Y. Hou, and C. M. Xia, “Design and Characterization of Bio-Chemical Sensor Based on Photonic Crystal Fiber with Fluorine-Doped Tin Oxides Film,” Plasmonics **14**(1) 197-203 (2019).
39. C. Liu, L. Yang, X. L. Lu, Q. Liu, F. M. Wang, J. W. Lv, T. Sun, H. W. Mu, and P. K. Chu, “Mid-infrared surface plasmon resonance sensor based on photonic crystal fiber,” Opt. Express **25**(13) 14227-14237 (2017).
40. Y. L. Cui, W. Huang, Z. F. Wang, M. L. Wang, Z. Y. Zhou, Z. X. Li, S. F. Gao, Y. Y. Wang, and P. Wang, “4.3 µm fiber laser in CO^2-filled hollow-core silica fibers,” Optica **6**(8) 951-954 (2019).
41. F. Maes,V. Fortin, S. Poulain, M.Poulain, J. Y. Carrée, M. Bernier, and R. Vallée, “Room-temperature fiber laser at 3.92 µm,” Optica **5**(7) 761-764 (2018).
42. Y. W. Qu, J. H. Yuan, X. Zhou, F. Li, B. B. Yan, Q. Wu, K. R. Wang, X. Z. Sang, K. P. Long, and C. X. Yu, “Mid-infrared silicon photonic crystal fiber polarization filter based on surface plasmon resonance effect,” Opt. Commun. **463** 125387 (2020).
43. Q. Liu, L. Xing, Z. X. Wu, L. Cai, Z. R. Zhang, and J. C. Zhao, “High-sensitivity photonic crystal fiber force sensor based on Sagnac interferometer for weighing,” Opt. Laser Technol. **123** 105939 (2020).
44. R. M. O. Jr, N. C. Panoiu, J. I. Dadap, X. P. Liu, X. G. Chen, I. W. Hsieh, E. Dulkeith, W. M. J. Green, and Y. A. Vlasov, “Engineering nonlinearities in nanoscale optical systems: physics and applications in dispersion-engineered silicon nanophotonic wires,” Adv. Opt. Photo. **1** 162-235 (2009).
45. Y. W. Qu, J. H. Yuan, X. Zhou, F. Li, C. Mei, B. B. Yan, Q. Wu, K. R. Wang, X. Z. Sang, K. P. Long, and C. X. Yu, “A V-shape photonic crystal fiber polarization filter based on surface plasmon resonance effect,” Opt. Commun. **452** 1-6 (2019).
46. E. R. Vera, J. Restrepo, C. J. Durango, J. M. Cardona, and N. G. Cardona, “Design of Low-loss and Highly Birefringent Porous-Core Photonic Crystal Fiber and Its Application to Terahertz Polarization Beam Splitter,” IEEE Photo. J. **10**(4) 5900413 (2018).
47. J. S. Wang, L. Pei, S. J. Weng, L. Y. Wu, J. Li, and T. G. Ning, “Ultrashort polarization beam splitter based on liquid-filled dual-core photonic crystal fiber,” Appl. Opt. **57**(14) 3847-3852 (2018).
48. C. Dou, X. L. Jing, S. G. Li, J. J. Wu, and Q. B. Wang, “A compact and low-loss polarization splitter based on dual-core photonic crystal fber,” Opt. Quant. Electron. **50** 255 (2018).
49. H. Y.Wang, X, Yan, S. G. Li, and X. N. Zhang, “Tunable surface plasmon resonance polarization beam splitter based on dual-core photonic crystal fiber with magnetic fluid,” Opt. Quant. Electron. **49** 368 (2017).
50. S. S. Zhang, W. G. Zhang, P. C. Geng, X. L. Li, and J. Ruan, “Design of single-polarization wavelength splitter based on photonic crystal fiber,” Appl. Opt. **50**(36) 6576-6582 (2011).
51. Z. H. Zhang, Y. F. Shi, B. M. Bian, and J. Lu, “Dependence of leaky mode coupling on loss in photonic crystal fiber with hybrid cladding,” Opt. Express **16**(3) 1915-1922 (2008).

52. A. Khaleque, E. G. Mironov, and H. T. Hattori, “Analysis of the properties of a dual-core plasmonic photonic crystal fiber polarization splitter,” Appl. Phys. B **121** 523-532 (2015).
53. F. Yaman, H. Pang, X. B. Xie, P. LiKamWa, and G. F, Li, “Silicon Photonic Crystal Fiber,” in Conference on Lasers and Electro-Optics/International Quantum Electronics Conference, OSA Technical Digest (CD) (Optical Society of America, 2009), paper CTuDD7.
54. Y. Li, K. Itoh, W. Watanabe, K. Yamada, D. Kuroda, J. Nishii, and Y. Y. Jiang, “Three-dimensional hole drilling of silica glass from the rear surface with femtosecond laser pulses,” Opt. Lett. **26**(23) 1912-1914 (2001).
55. C. Hong, H. Kim, S. Park, and C. Lee, “Optical properties of porous silicon coated with ultrathin gold film by RF-magnetron sputtering,” J. Eur. Ceram. Soc. **30** 459-463 (2010).
56. X. Zhang, R. Wang, F. M. Cox, B.T. Kuhlmey, and M. C. J. Large, “Selective coating of holes in microstructured optical fiber and its application to in-fiber absorptive polarizers,” Opt. Express **15**(24) 16270-16278 (2007).
57. B. Y. Li, Z. C Sheng, M. Wu, X. Y. Liu, G. Y. Zhou, J. T. Liu, Z. Y. Hou, and C. M. Xia, “Sensitive real-time monitoring of refractive indices and components using a microstructure optical fiber microfluidic sensor,” Opt. Lett. **43**(20) 5070-5073 (2018).
58. P. J. A. Sazio, A. A. Correa, C. E. Finlayson, J. R. Hayes, T. J. Scheidemantel, N. F. Baril, B. R. Jackson, D. J. Won, F. Zhang, E. R. Margine, V. Gopalan, V. H. Crespi, and J. V. Badding, “Microstructured Optical Fibers as High-Pressure Microfluidic Reactors,” Science **311** 1583-1586 (2006).
59. T. S. Wu, Y. Shao, Y. Wang, S. Q. Cao, W. P. Cao, F. Zhang, C. R. Liao, J. He, Y. J. Huang, M. X. Hou, and Y. P. Wang, “Surface plasmon resonance biosensor based on gold-coated side-polished hexagonal structure photonic crystal fibe,” Opt. Express **25**(17) 20313-20322 (2017).
60. Y. Wang, Q. Huang, W. J. Zhu, M. H. Yang, and E. Lewis, “Novel optical fiber SPR temperature sensor based on MMF-PCF-MMF structure and gold-PDMS film,” Opt. Express **26**(2) 1910-1917 (2018).